# Continuous Low-Bias Switching of Superconductivity in a MoS2 Transistor

Chen, Qihong; Lu, Jianming; Liang, Lei; Zheliuk, Oleksandr; El Yumin, Abdurrahman Ali; Ye, Jianting

*Published in:*
Advanced materials

*DOI:*
10.1002/adma.201800399



*Publication date:*
2018

ADVANCED MATERIALS
www.advmat.de

# Continuous Low-Bias Switching of Superconductivity in a $MoS_2$ Transistor

*Qihong Chen,* Jianming Lu, Lei Liang, Oleksandr Zheliuk, Abdurrahman Ali El Yumin, and Jianting Ye**

**Engineering the properties of quantum electron systems, e.g., tuning the superconducting phase using low driving bias within an easily accessible temperature range, is of great interest for exploring exotic physical phenomena as well as achieving real applications. Here, the realization of continuous field-effect switching between superconducting and non-superconducting states in a few-layer $MoS_2$ transistor is reported. Ionic-liquid gating induces the superconducting state close to the quantum critical point on the top surface of the $MoS_2$, and continuous switching between the super/non-superconducting states is achieved by $HfO_2$ back gating. The superconducting transistor works effectively in the helium-4 temperature range and requires a gate bias as low as ≈10 V. The dual-gate device structure and strategy presented here can be easily generalized to other systems, opening new opportunities for designing high-performance 2D superconducting transistors.**

Switching between superconducting and non-superconducting states has been widely studied in low-dimensional superconducting systems by adjusting static parameters such as film thickness,[1] disorder[2] as well as chemical doping.[3] Alternative tunable parameter, best exemplified by field effect gating, is increasingly used as a continuous switching knob to control superconductivity in systems with given chemical stoichiometry and disorder morphology. A superconducting field effect transistor (SuFET), which has virtually loss-free transistor channels, has been a long-pursued goal for device applications.[4] Limited by the fact that switching superconductivity on and off usually requires tuning carriers in large amount, previous efforts were mostly focused on maximizing field effect by using special gate dielectrics such as ferroelectric[5] and quantum paraelectric,[6] e.g., superconductivity at the $LaAlO_3/SrTiO_3$ interface can be completely switched on and off by applying gate voltages to the backside of $SrTiO_3$ substrate. However, even with the large dielectric constant of $SrTiO_3$, continuous switching between superconducting and non-superconducting states at the $LaAlO_3/SrTiO_3$ interface usually requires gate voltages as high as hundreds of volts. Also, the very low superconducting transition temperature[6–8] limited the $SrTiO_3$ SuFET to helium-3 based cryogenic systems, which is far more complicated than the very mature and widely available helium-4 based cryogenic techniques.

Recently, field effect doping by electrical double layer (EDL) has been demonstrated as an effective method for inducing and manipulating large amount of carriers.[9–11] With this technique, superconductivity can be routinely induced in 2D transition metal dichalcogenides (TMDs) such as $MoS_2$,[12–14] $MoSe_2$,[15] $MoTe_2$,[15] and $WS_2$.[16] Superconductivity at the TMD/liquid interface behaves as a 2D system with inversion symmetry broken by the electric field,[17] which induces an effective Zeeman field that strongly protects the superconductivity against large in-plane magnetic field.[17–19] Besides TMDs, ionic gating has also been proved to be effective in manipulating high temperature superconductivity in copper oxides. Complete on/off switching of superconductivity was realized in $La_{2-x}Sr_xCuO_4$[20] and $YBa_2Cu_3O_{7-x}$,[21] etc. In spite of the high capability in tuning carrier density, ionic gating functions only when the ions are mobile above the glass transition temperature of the ionic media. Devices have to be warmed up to high temperature (usually close to the room temperature or slightly lower) in order to change the doping profile. Therefore, the lack of continuous tunability below the superconducting transitions of ion-gated SuFET sets the major barrier to any real applications. Realizing continuous tuning of SuFET requires not only new ways of incorporating the existing superconducting systems but also alternative device concepts.

In this work, we show that a SuFET can be realized in $MoS_2$ by combining the advantages of ionic-liquid and solid-state gating. Ionic liquid as top gate induces superconductivity at the surface of $MoS_2$. By carefully tuning the liquid gate voltage and positioning the superconducting state close to the quantum critical

Dr. Q. Chen, Dr. L. Liang, O. Zheliuk, A. Ali El Yumin, Prof. J. Ye
Device Physics of Complex Materials
Zernike Institute for Advanced Materials
University of Groningen
Groningen 9747 AG, The Netherlands
E-mail: qihong.chen@rug.nl; j.ye@rug.nl
Dr. J. Lu
State Key Laboratory for Mesoscopic Physics
Peking University
Beijing 100871, P. R. China
The ORCID identification number(s) for the author(s) of this article can be found under https://doi.org/10.1002/adma.201800399.



**DOI: 10.1002/adma.201800399**

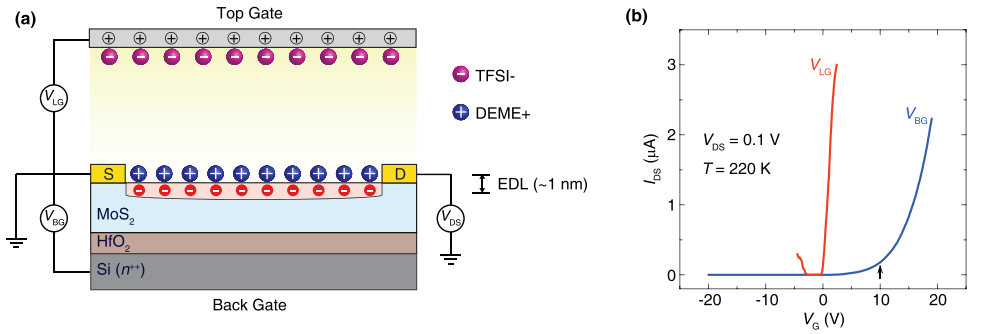


**Figure 1.** a) Device configuration of a dual-gate $MoS_2$ transistor. Electrical double layer (EDL) mainly induces carriers at the top surface of $MoS_2$, highlighted by pink color. b) Transfer curves by ionic-liquid gate ($V_{LG}$, orange) and $HfO_2$ back gate ($V_{BG}$, blue), respectively, at $T = 220$ K with source–drain voltage $V_{DS} = 0.1$ V.

point (QCP, the onset of superconductivity), a high efficiency back gate (based on high-$\kappa$ dielectric $HfO_2$) can continuously change the state across the phase boundaries at low temperatures. At small back gate voltages, the change of transition temperature ($T_c$) agrees well with the phase diagram,[12] whereas a significant deviation is observed at relatively large back gate voltages. This behavior can be understood using a two-channel model, in which the superconductivity exists exclusively in the topmost layer and back gate can induce a metallic state in the bottom layers. The topmost superconducting layer and bottom metallic layers form two parallel conducting channels, and the interaction between them leads to the proximity effect that suppresses the superconductivity. Compared to previous systems, owing to the pure solid gating and precise positioning of the superconducting ground state, our $MoS_2$-SuFET can achieve continuous switching similar to a typical solid-state transistor, requires only a small gate voltage of ≈10 V and works in the helium-4 temperature range with $T_c \approx 7$ K, therefore it serves as an ideal platform for studying superconductivity in 2D systems.

**Figure 1**a shows the device configuration of a $MoS_2$-SuFET. The data in the main text of this study are from the same device fabricated on a $HfO_2$ (50 nm)/Si ($n^{++}$) substrate. The $MoS_2$ flake is 2.5 nm thick, composed of four monolayers (see Figure S1, Supporting Information). Back gate dielectrics $HfO_2$ (50 nm thick, dielectric constant ≈20) was deposited by atomic layer deposition (ALD) on a highly doped silicon substrate. For ionic-liquid gating, we used the well-known ionic liquid: *N*,*N*-diethyl-*N*-(2-methoxyethyl)-*N*-methylammonium bis-(trifluoromethylsulfonyl)-imide (DEME-TFSI). The gating procedure was conducted at low temperature ($T$ = 220 K) to avoid chemical reaction. The transfer curve by ionic gating (Figure 1b, orange curve) shows ambipolar transistor operation. $MoS_2$ becomes superconducting when a positive voltage bias ($V_{LG}$) is applied and cool down to low temperatures. The induced 2D electron density ($n_{2D}$) is generally in the range of ≈$10^{14}$ cm$^{-2}$. On the other hand, back gate bias ($V_{BG}$) can be applied up to ±20 V with leak current less than 1 nA, reaching a continuous carrier density tuning of $\pm 4 \times 10^{13}$ cm$^{-2}$. As can be seen from the transfer curve by back gate in Figure 1b (blue curve), a negative or small positive $V_{BG}$ (<10 V) is not able to switch on the $MoS_2$ channel. At relatively large $V_{BG}$ (>10 V), carriers start to accumulate in the $MoS_2$ channel hence conductivity increases.

By carefully adjusting $V_{LG}$, we prepared a superconducting state close to the QCP. At this state, the carrier density is ≈$6 \times 10^{13}$ cm$^{-2}$ according to the well-established phase diagram.[12] At low temperatures, the superconductivity can be effectively tuned by $V_{BG}$, as can be seen in **Figure 2**. Figure 2a shows the temperature dependence of the sheet resistance $R_s$ measured at different $V_{BG}$ between −20 and 20 V. At largest negative $V_{BG}$ thus lowest $n_{2D}$, $dR_s/dT < 0$ indicates an insulating behavior.[22] Increasing $V_{BG}$ gradually switches on the superconductivity and the transition temperature $T_c$ increases with increasing $V_{BG}$. Here $T_c$ is defined as 50% of the normal state resistance $R_N$ ($R_s$ at $T$ = 13 K). The evolution of superconductivity is plotted in a quasicontinuous 2D map as a function of temperature and $V_{BG}$ in Figure 2b, where the super/non-superconducting phase boundary, i.e., the borderline between orange/green areas, can be freely accessed by varying $V_{BG}$. It should be noted that for negative $V_{BG}$, the $n_{2D}$ spans approximately from 2 to $6 \times 10^{13}$ cm$^{-2}$, where a metallic state should be observed according to the phase diagram.[12,23] The observed insulating behavior can be attributed to the reduced localization length due to ionic doping inhomogeneity or disorders, which leads to a crossover from weak to strong localization. Similar insulating behavior was also observed in $SrTiO_3$ electrical double layer transistor (EDLT) device due to Kondo effect,[24] but it is unlikely to happen in our system in absence of any localized magnetic ions.

The 2D superconducting transition can be well described by the Berezinskii–Kosterlitz–Thouless (BKT) behavior,[6,25] in which the temperature dependence of $R_s$ has the following form above the critical temperature $T_{BKT}$, $R_s(T) \propto \exp(-\frac{b}{\sqrt{T - T_{BKT}}})$, where $b$ is a constant related to the vortex–antivortex interaction strength. In Figure 2c, we plot $(d\ln R/dT)^{-2/3}$ as a function of $T$ for back gate $V_{BG}$ = 20 V. Consistency with the BKT scenario can be established by the linear behavior close to $T_{BKT}$ determined by the condition $(d\ln R/dT)^{-2/3} = 0$. The extracted $T_{BKT}$ for other $V_{BG}$ is shown in Figure 2d (dark blue dots). Accessing the QCP is well controlled by $V_{BG}$, and $T_{BKT} = 0$ is found at a critical back gate of $V_{GC} = -1$ V. The related variation of carrier concentration $\Delta n_{2D} = n - n_c$ serves as a direct control parameter for superconductor-insulator transition, where $n_c$ denotes the critical carrier density at QCP. Following the scaling theory of superconductor-insulator transition,[26] $T_{BKT}$ is expected to scale near the QCP as $T_{BKT} \propto (\delta n_{2D})^{z\nu} \propto (\delta V)^{z\nu}$, where $z\nu$ is the scaling factor, and $\delta n_{2D}$ the variation of $n_{2D}$ which is proportional to $\delta V = V - V_{GC}$. In Figure 2d, we can see that $T_{BKT}$ can be well described by $T_{BKT} \propto (\delta V)^{z\nu}$, with $z\nu = 2/3$, which is consistent with the 2D-XY model at nonzero temperatures.[27] Similar values were also obtained for superconductivity in amorphous bismuth film[22] and at the $LaAlO_3/SrTiO_3$ interface.[6]

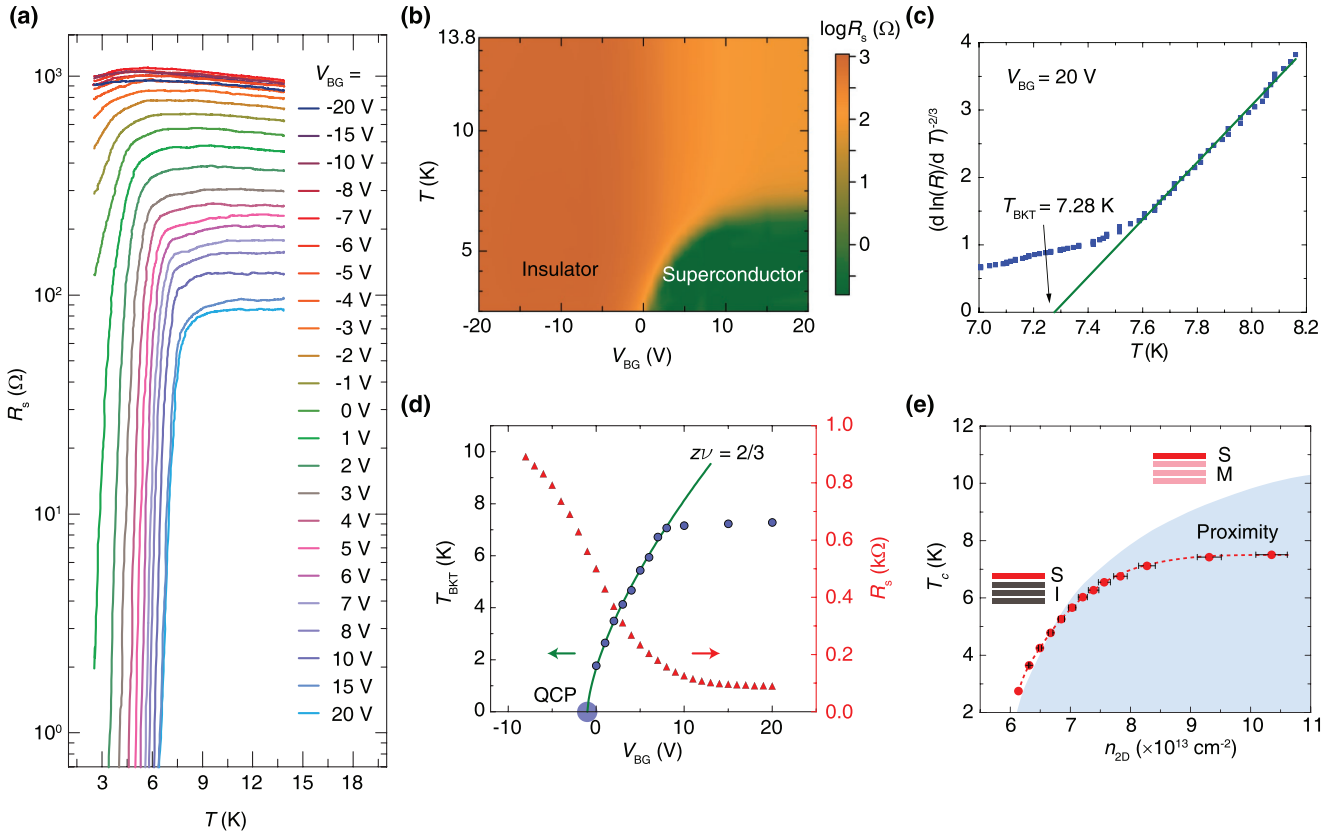


**Figure 2.** a) Temperature dependence of the sheet resistance $R_s$ for different $V_{BG}$ between –20 and 20 V. b) A 2D color map of logarithm of $R_s$ as a function of temperature and back gate bias, showing the evolution between superconducting (green) and insulating (orange) phases. c) $[d\ln(R)/dT]^{-2/3}$ plotted as a function of temperature, with $V_{BG} = 20$ V. The solid line is the behavior expected for a BKT transition with $T_{BKT} = 7.28$ K. d) Left axis shows changes of $T_{BKT}$ as a function of $V_{BG}$. The green solid line describes the scaling relationship $T_{BKT} \propto (V - V_c)^{z\nu}$, where $z\nu = 2/3$. Red triangular dots show the $V_{BG}$ dependence of normal state $R_s$ measured at $T = 13$ K. e) Transition temperature $T_c$ (red dots) as a function of 2D carrier density $n_{2D}$. Dashed red line is a guidance for eyes, shaded area represents the phase diagram from ref. [12] The error bars indicate the uncertainties from the capacitance of $HfO_2$. Two small insets represent different states of the bottom channel at different range of $V_{BG}$, "SC," "I," and "M" stand for superconducting, insulating, and metallic, respectively.

At $V_{BG} > 10$ V, the variation of $T_{BKT}$ deviates from the scaling theory. This behavior is accompanied by the saturation of normal state resistance (measured at 13 K), as can be seen in Figure 2d (red triangles): $R_s$ decreases rapidly at $V_{BG} < 10$ V, whereas a clear saturation of $R_s$ is observed at $V_{BG} > 10$ V. Motivated by this unusual behavior, we map our data to the established phase diagram[12] in Figure 2e. The carrier density $n_{2D}$ is determined by $n_{2D} = n_c + C_g(V_{BG} - V_{GC})$. Here $n_c = 6 \times 10^{13}$ cm$^{-2}$ is the carrier density at QCP,[12] $C_g = 350$ nF cm$^{-2}$ the capacitance of $HfO_2$ per unit area, and $V_{GC} = -1$ V the critical back gate voltage. As can be seen in Figure 2e, at small $V_{BG}$ the change of $T_c$ ($T_c$ as a function of $n_{2D}$) is well mapped to the phase diagram, whereas a growing deviation is observed at higher $V_{BG}$.

It is well known that the distribution of carriers induced by ionic gating decays exponentially from the top to bottom due to the strong Thomas–Fermi screening effect.[17,28–30] Nearly 90% of the carriers induced by ionic gating are confined to the topmost layer, which becomes electronically isolated from the rest of layers below and acts like a freestanding monolayer. The bottom layers are not affected by ionic gating. Back gating induces smaller amount of carriers compared to ionic gating. The induced carriers decrease from the bottom to top also due to the screening effect, thus the carriers induced by back gate preferentially couple to the bottom layers.[30,31] According to the transfer curve in Figure 1b, negative or small positive $V_{BG}$ are not able to induce carriers in the bottom layers, hence the bottom layers simply act as an additional dielectric layer for the field effect of back gate. Higher positive $V_{BG}$ starts to accumulate carriers in the bottom layers which form another conducting channel. Nevertheless, the carrier density induced by back gate is not high enough for the bottom layers to reach the superconducting phase, therefore the bottom layers are in normal metallic state. In other words, two parallel conducting channels form due to ionic and back gating: the top superconducting channel and the bottom normal channel. The existence of these two parallel conducting channels have been confirmed by the observation of both superconductivity and Shubnikov–de Haas quantum oscillations in the same device, contributed by the top and bottom channels, respectively.[30] When a metallic state is established in the bottom channel at large $V_{BG}$, our device becomes an analogue of a superconductor sitting on a normal metal. In a conventional superconductor-normal metal (SN) sandwich structure, the $T_c$ of a superconducting thin film

is reduced due to the proximity effect between the superconductor and normal metal.[32–37] On one hand, higher $V_{BG}$ adds more electrons to the topmost superconducting layer, therefore $T_c$ should increase; on the other hand, the bottom channel becomes more metallic at higher $V_{BG}$, leading to stronger proximity effect, thus $T_c$ should be suppressed. Overall, the measured $T_c$ saturates at $V_{BG} > 10$ V due to the competition between these two effects. Similar behavior is observed in another device (see Figure S5, Supporting Information). Therefore, the deviation of $T_c$ from the phase diagram is attributed to the proximity effect between the top superconducting layer and bottom normal layers. Furthermore, the proximity effect also introduces some unusual behavior in the upper critical field, which will be elaborated below.

Temperature dependence of the perpendicular ($B\perp ab$) and parallel ($B\|ab$) upper critical field $B_{c2}$ is closely associated with the change of $T_c$. In 2D Ginzburg–Landau model, the perpendicular and parallel critical fields are phenomenologically described by[38]

$$B_{c2}^{\perp}(t) = \frac{\Phi_0}{2\pi\xi_{GL}(0)^2}(1-t) \quad (1)$$

and

$$B_{c2}^{\parallel}(t) = \frac{\Phi_0\sqrt{12}}{2\pi\xi_{GL}(0)d_T}(1-t)^{\frac{1}{2}} \quad (2)$$

where $t = T/T_c$ denotes the reduced temperature, $\Phi_0 = \frac{h}{2e} = 2.07 \times 10^{-15}$ Wb is the flux quantum, $\xi_{GL}(0)$ is the Ginzburg–Landau coherence length at zero temperature, $d_T$ is the effective thickness of superconductivity. The temperature dependence of perpendicular critical field is shown in **Figure 3**a, where $B_{c2}^{\perp} - T_c$ show linear relation close to the transition temperature as depicted by the solid lines, in good agreement with the 2D Ginzburg–Landau model. The extracted coherence length $\xi_{GL}(T = 0\ \text{K})$ decreases with the increase of $V_{BG}$, as shown in the inset of Figure 3a. With $V_{BG}$ changing from 2 to 15 V, the slope of the $B_{c2}^{\perp} - T_c$ curve increases, suggesting higher critical field with increasing $T_c$.[39,40] However, a crossover is observed for the curves of $V_{BG} = 15$ and 20 V, as highlighted by the yellow dot in Figure 3a, suggesting a lower $B_{c2}^{\perp}$ with higher $T_c$ at $V_{BG} = 20$ V. This behavior can be qualitatively understood by the Werthamer–Helfand–Hohenberg (WHH) theory.[41] The slope of the temperature dependence of $B_{c2}$ at $T_c$, $\frac{dB_{c2}^{\perp}}{dT}|_{T=T_c}$, is inversely correlated with the electron mean free path. Longer mean free path corresponds to lower critical field. In our device at relatively large $V_{BG}$, the bottom layers enter a metallic state and act as an effective screening layer that reduces the charged impurity scatterings in the topmost superconducting layer. As a result, the electron mean free path increases significantly, leading to the reduction of $B_{c2}$.

Figure 3b shows the temperature dependence of the upper critical field parallel to the *ab*-plane of $MoS_2$ and the dashed lines show the corresponding fitting by the 2D Ginzburg–Landau model. The parallel critical field can easily exceed the Pauli limit $B_p \approx 1.86\ T_c(0)$, which is indicated by the shaded area in Figure 3b. With the extracted parallel critical field at zero temperature, we could estimate the effective thickness of the superconductivity by Tinkham model $d_T$ as shown in the inset of Figure 3b. The extracted $d_T$ is much smaller than $\xi_{GL}$, indicating the 2D nature of superconductivity. It should be noted that $d_T$ tends to overestimate the thickness of superconducting layer since the estimated $d_T$ is even larger than the thickness of the $MoS_2$ flake. This is because the Tinkham model does not consider spin–orbit interaction or Pauli paramagnetism, both of which are essential in our devices. Therefore, $d_T$ estimated here is an upper limit of the thickness of superconducting layer, consistent with previous reports.[42,43] Nevertheless, the relative change of $d_T$ at different $V_{BG}$ provides valuable information about the behavior of superconductivity. $d_T$ first increases with the increase of $V_{BG}$, suggesting a more robust superconducting state; whereas the reduction of $d_T$ at $V_{BG} > 10$ V agrees with the scenario that the proximity effect between the metallic bottom layers and the superconducting top layer weakens the superconductivity.

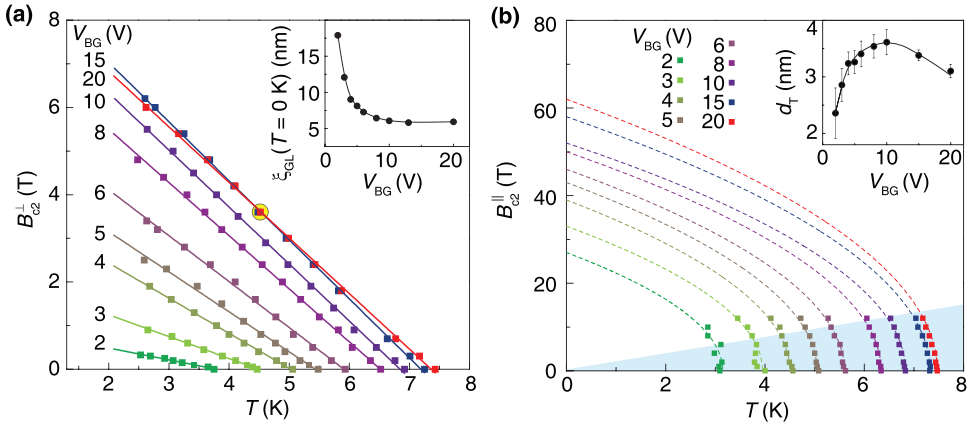


**Figure 3.** a) Temperature dependence of $B_{c2}$ perpendicular to the *ab*-plane of $MoS_2$, at different $V_{BG}$. Solid lines are the best linear fittings. Inset: Extracted coherence length at $T = 0$ K as a function of gate voltage. b) Temperature dependence of $B_{c2}$ parallel to the *ab*-plane of $MoS_2$, at different $V_{BG}$. Dashed lines are the best fittings using 2D Ginzburg–Landau model. Inset: Extracted effective thickness of the superconductivity $d_T$ as a function of $V_{BG}$, solid line is a guidance for eyes.

It should be noted that in this study we only focus on $MoS_2$ flakes with thicknesses of 4–5 monolayers. Previous discussions have shown that the carrier density induced by ionic-liquid gating decays exponentially from the top to bottom due to the strong screening effect, hence the gating effect only extends to 2–3 layers from the top surface and most of the total induced carriers concentrates in the topmost layer.[17,28–30] In contrast, back gating induces smaller amount of carriers but the gating effect extends to more layers from the bottom surface. Therefore, for very thick flakes,[44,45] it is possible to form the superconducting-insulating-metallic channels and no interaction between the superconducting top surface and metallic bottom surface is expected. The middle insulating channel serves as an additional dielectric layer for the field effect tuning of the superconductivity on the top surface. Negative back gate can still tune the superconductivity by depleting the carriers on the top surface, while the tuning capability of positive back gate is largely reduced since it accumulates carriers mainly on the bottom surface. For few-layer flakes (4–5 layers) discussed in this study, they have independent superconducting top surface and metallic bottom surface. Meanwhile, we can also observe the interaction between them. For even thinner flakes (≤3 layers) it becomes more complicated because of the interlayer coupling, screening and charge impurity scattering from substrate, etc. For example, monolayer $WS_2$ exhibits a complete set of competitive electronic phases range from a band insulator, a superconductor, to an unexpected re-entrant insulator.[46] A systematic study of $MoS_2$ flakes with different layer numbers is required to understand the thickness effect on the electrical properties.

Finally, we compare our transistor with other materials/devices reported to exhibit quantum phase transition (QPT) by field effect tuning, as shown in **Figure 4**. From application perspective, it is highly demanded to realize superconducting transistors that can operate continuously at high temperatures and with low gate voltages, corresponding to the top left corner of the diagram. The high $T_c$ cuprate, $YBa_2Cu_3O_{7-x}$ film[21] is the closest to this goal but the QPT is realized by ionic-liquid gating, which does not function below the superconducting transition. This disadvantage also exists in $LaSrCuO_4$ film[20] and ZrNCl thin flake[47] with relatively high transition temperatures but realized by ionic gating as well. Amorphous bismuth[22] and $LaAlO_3/SrTiO_3$[6–8] can achieve continuous QPT but they either work at very low temperature or require gate voltage as high as hundreds of volts. Proximity induced superconductivity in metal decorated graphene[48] can be tuned at low temperatures with moderate gate voltages by controlling the channel transmittance for cooper pairs without turning the channel material into a superconductor, therefore it is not able to withstand large supercurrent. Compared with previous materials, our $MoS_2$ superconducting transistor can work in the helium-4 temperature range with continuous control of the superconducting phase transition and only requires gate voltage as low as ≈10 V. The combination of ionic-liquid gating and $HfO_2$ back gating presented in this work demonstrates an excellent candidate for balancing basic research and possible applications.

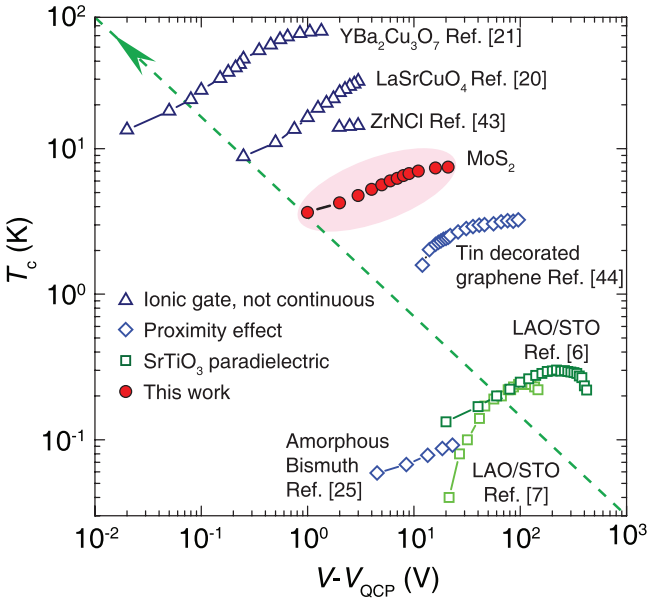


**Figure 4.** Comparison of the performance of $MoS_2$-EDLT superconducting transistor with other reported systems that are capable of tuning superconductivity. The present device made of multilayer $MoS_2$ flakes has the advantages of continuous operation, working in the helium-4 temperature range and with low bias (≈10 V).

## Experimental Section

*Device Fabrication*: Thin $MoS_2$ flakes were prepared by micromechanically exfoliating bulk single crystals of 2H polytype (SPI supplies), and then transferred to a silicon wafer with 50 nm $HfO_2$, which was deposited by ALD. Optical microscopy and atomic force microscopy (AFM) were used to select thin and uniform flakes for device fabrication. Electrodes composed of Ti/Au (5 nm/65 nm) were deposited in a high vacuum electron beam evaporator, after patterning by standard e-beam lithography. After electrode deposition, the whole sample flake and gate electrode were immersed in a small droplet of ionic liquid: DEME-TFSI.

*Electrical Measurement*: For transport measurement, liquid top and solid back gate voltages were set by a Keithley 2450 DC source meter. Transport properties at low temperatures were measured in a helium-4 based cryogen free system (Cryogenic UK). Sample resistance was taken by measuring voltage drops across the sample with a constant AC current, using standard lock-in amplifiers (Stanford Research SR830). *I–V* curves were measured with Keithley 2450 DC meter.

## Supporting Information

Supporting Information is available from the Wiley Online Library or from the author.

## Acknowledgements

The authors thank J. Harkema and A. Joshua for technical support. Q.C. thanks the scholarship from The Ubbo Emmius Fund. J.Y. and Q.C. thank the Stichting voor Fundamenteel Onderzoek der Materie (FOM, FV157) and FlagERA iSpinText for financial support. J.Y. acknowledges funding from the European Research Council (consolidator Grant No. 648855, Ig-QPD).

Note: The presentation of the initials of author Abdurrahman Ali El Yumin was corrected on July 9, 2018, after initial publication online.

## Conflict of Interest

The authors declare no conflict of interest.

## Keywords

continuous operation, ionic gating, low-bias switching, superconducting transistors, transition metal dichalcogenides

Received: January 18, 2018
Revised: March 9, 2018
Published online: May 28, 2018

[1] D. B. Haviland, Y. Liu, A. M. Goldman, *Phys. Rev. Lett.* **1989**, *62*, 2180.
[2] J. M. Graybeal, M. R. Beasley, *Phys. Rev. B* **1984**, *29*, 4167.
[3] H. Takagi, T. Ido, S. Ishibashi, M. Uota, S. Uchida, Y. Tokura, *Phys. Rev. B* **1989**, *40*, 2254.
[4] J. Mannhart, *Supercond. Sci. Technol.* **1996**, *9*, 49.
[5] K. S. Takahashi, M. Gabay, D. Jaccard, K. Shibuya, T. Ohnishi, M. Lippmaa, J.-M. Triscone, *Nature* **2006**, *441*, 195.
[6] A. D. Caviglia, S. Gariglio, N. Reyren, D. Jaccard, T. Schneider, M. Gabay, S. Thiel, G. Hammerl, J. Mannhart, J.-M. Triscone, *Nature* **2008**, *456*, 624.
[7] J. Biscaras, N. Bergeal, S. Hurand, C. Feuillet-Palma, A. Rastogi, R. C. Budhani, M. Grilli, S. Caprara, J. Lesueur, *Nat. Mater.* **2013**, *12*, 542.
[8] P. D. Eerkes, W. G. van der Wiel, H. Hilgenkamp, *Appl. Phys. Lett.* **2013**, *103*, 201603.
[9] H. Yuan, H. Shimotani, A. Tsukazaki, A. Ohtomo, M. Kawasaki, Y. Iwasa, *Adv. Funct. Mater.* **2009**, *19*, 1046.
[10] S. Ono, N. Minder, Z. Chen, A. Facchetti, A. F. Morpurgo, *Appl. Phys. Lett.* **2010**, *97*, 143307.
[11] K. Hong, S. H. Kim, K. H. Lee, C. D. Frisbie, *Adv. Mater.* **2013**, *25*, 3413.
[12] J. T. Ye, Y. J. Zhang, R. Akashi, M. S. Bahramy, R. Arita, Y. Iwasa, *Science* **2012**, *338*, 1193.
[13] D. Costanzo, S. Jo, H. Berger, A. F. Morpurgo, *Nat. Nanotechnol.* **2016**, *11*, 339.
[14] Q. Chen, L. Liang, A. Ali El Yumin, J. Lu, O. Zheliuk, J. Ye, *Phys. Status Solidi B* **2017**, *00*, 1700181.
[15] W. Shi, J. Ye, Y. Zhang, R. Suzuki, M. Yoshida, J. Miyazaki, N. Inoue, Y. Saito, Y. Iwasa, *Sci. Rep.* **2015**, *5*, 12534.
[16] S. Jo, D. Costanzo, H. Berger, A. F. Morpurgo, *Nano Lett.* **2015**, *15*, 1197.
[17] J. M. Lu, O. Zheliuk, I. Leermakers, N. F. Q. Yuan, U. Zeitler, K. T. Law, J. T. Ye, *Science* **2015**, *350*, 1353.
[18] Y. Saito, Y. Nakamura, M. S. Bahramy, Y. Kohama, J. Ye, Y. Kasahara, Y. Nakagawa, M. Onga, M. Tokunaga, T. Nojima, Y. Yanase, Y. Iwasa, *Nat. Phys.* **2016**, *12*, 144.
[19] X. Xi, Z. Wang, W. Zhao, J.-H. Park, K. T. Law, H. Berger, L. Forró, J. Shan, K. F. Mak, *Nat. Phys.* **2016**, *12*, 139.
[20] A. T. Bollinger, G. Dubuis, J. Yoon, D. Pavuna, J. Misewich, I. Božović, *Nature* **2011**, *472*, 458.
[21] X. Leng, J. Garcia-Barriocanal, S. Bose, Y. Lee, A. M. Goldman, *Phys. Rev. Lett.* **2011**, *107*, 027001.
[22] K. A. Parendo, K. H. S. B. Tan, A. Bhattacharya, M. Eblen-Zayas, N. E. Staley, A. M. Goldman, *Phys. Rev. Lett.* **2005**, *94*, 197004.
[23] X. Chen, Z. Wu, S. Xu, L. Wang, R. Huang, Y. Han, W. Ye, W. Xiong, T. Han, G. Long, Y. Wang, Y. He, Y. Cai, P. Sheng, N. Wang, *Nat. Commun.* **2015**, *6*, 6088.
[24] M. Lee, J. R. Williams, S. Zhang, C. D. Frisbie, D. Goldhaber-Gordon, *Phys. Rev. Lett.* **2011**, *107*, 256601.
[25] N. Reyren, S. Thiel, A. D. Caviglia, L. F. Kourkoutis, G. Hammerl, C. Richter, C. W. Schneider, T. Kopp, A.-S. Rüetschi, D. Jaccard, M. Gabay, D. A. Muller, J.-M. Triscone, J. Mannhart, *Science* **2007**, *317*, 1196.
[26] T. Schneider, *Acta Phys. Pol., A* **1997**, *1*, 203.
[27] S. L. Sondhi, S. M. Girvin, J. P. Carini, D. Shahar, *Rev. Mod. Phys.* **1997**, *69*, 315.
[28] N. T. Cuong, M. Otani, S. Okada, *J. Phys.: Condens. Matter* **2014**, *26*, 135001.
[29] R. Roldán, E. Cappelluti, F. Guinea, *Phys. Rev. B* **2013**, *88*, 054515.
[30] Q. H. Chen, J. M. Lu, L. Liang, O. Zheliuk, A. Ali, P. Sheng, J. T. Ye, *Phys. Rev. Lett.* **2017**, *119*, 147002.
[31] S. Das, J. Appenzeller, *Nano Lett.* **2013**, *13*, 3396.
[32] P. G. De Gennes, *Rev. Mod. Phys.* **1964**, *36*, 225.
[33] L. N. Cooper, *Phys. Rev. Lett.* **1961**, *6*, 689.
[34] W. L. McMillan, *Phys. Rev.* **1968**, *175*, 537.
[35] Y. V. Fominov, N. M. Chtchelkatchev, A. A. Golubov, *Phys. Rev. B* **2002**, *66*, 014507.
[36] J. Kim, Y.-J. Doh, K. Char, H. Doh, H.-Y. Choi, *Phys. Rev. B* **2005**, *71*, 214519.
[37] M. Wolz, C. Debuschewitz, W. Belzig, E. Scheer, *Phys. Rev. B* **2011**, *84*, 104516.
[38] M. Tinkham, *Phys. Rev.* **1963**, *129*, 2413.
[39] X. Xi, H. Berger, L. Forró, J. Shan, K. F. Mak, *Phys. Rev. Lett.* **2016**, *117*, 106801.
[40] M. Tinkham, *Introduction to Superconductivity*, 2nd ed., Dover Publications, Mineola, NY, USA **2004**.
[41] N. R. Werthamer, E. Helfand, P. C. Hohenberg, *Phys. Rev.* **1966**, *147*, 295.
[42] M. Ben Shalom, M. Sachs, D. Rakhmilevitch, A. Palevski, Y. Dagan, *Phys. Rev. Lett.* **2010**, *104*, 126802.
[43] M. Kim, Y. Kozuka, C. Bell, Y. Hikita, H. Y. Hwang, *Phys. Rev. B* **2012**, *86*, 085121.
[44] Y. Liu, J. Guo, Q. He, H. Wu, H.-C. Cheng, M. Ding, I. Shakir, V. Gambin, Y. Huang, X. Duan, *Nano Lett.* **2017**, *17*, 5495.
[45] S. Tran, J. Yang, N. Gillgren, T. Espiritu, Y. Shi, K. Watanabe, T. Taniguchi, S. Moon, H. Baek, D. Smirnov, M. Bockrath, R. Chen, C. N. Lau, *Sci. Adv.* **2017**, *3*, e1603179.
[46] J. M. Lu, O. Zheliuk, Q. H. Chen, I. Leermakers, N. E. Hussey, U. Zeitler, J. T. Ye, *Proc. Natl. Acad. Sci. USA* **2018**, *115*, 3551.
[47] J. T. Ye, S. Inoue, K. Kobayashi, Y. Kasahara, H. T. Yuan, H. Shimotani, Y. Iwasa, *Nat. Mater.* **2010**, *9*, 125.
[48] A. Allain, Z. Han, V. Bouchiat, *Nat. Mater.* **2012**, *11*, 590.